




A computational study on possible active species in nickel(II)-catalyzed 1-butene dimerization in [BMIM]⁺[AlCl₄]⁻ ionic liquid solution

Ioannis Nikiforidis, Andreas Göring & Wolfgang Hieringer

To cite this article: Ioannis Nikiforidis, Andreas Göring & Wolfgang Hieringer (2015) A computational study on possible active species in nickel(II)-catalyzed 1-butene dimerization in [BMIM]⁺[AlCl₄]⁻ ionic liquid solution, Journal of Coordination Chemistry, 68:17-18, 3362-3373, DOI: [10.1080/00958972.2015.1075015](https://doi.org/10.1080/00958972.2015.1075015)


To link to this article: <http://dx.doi.org/10.1080/00958972.2015.1075015>

 View supplementary material 

 Accepted author version posted online: 27 Jul 2015.
Published online: 21 Aug 2015.

 Submit your article to this journal 

 Article views: 50

 View related articles 

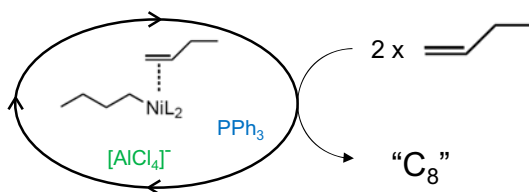
 View Crossmark data 

A computational study on possible active species in nickel(II)-catalyzed 1-butene dimerization in [BMIM]⁺[AlCl₄][−] ionic liquid solution

IOANNIS NIKIFORIDIS, ANDREAS GÖRLING and WOLFGANG HIERINGER*

Lehrstuhl für Theoretische Chemie and Interdisciplinary Center for Molecular Materials, Universität Erlangen-Nürnberg, 91058 Erlangen, Germany

(Received 27 March 2015; accepted 16 July 2015)



The butene insertion step of nickel complex-catalyzed butene dimerization in the presence of a [BMIM]⁺[AlCl₄][−] ionic liquid has been studied using density functional theory. The possibility of anion coordination from the ionic liquid to the catalyst complex has explicitly been taken into account. The calculated relative energies of various possible active catalyst complexes suggest that anion coordination to the nickel center may be thermodynamically favorable. Phosphine-free complexes which are only coordinated by one or two AlCl₄[−] anions are higher in energy and show higher activation barriers for butene insertion. The lowest activation barrier has been found for a mono-phosphine nickel complex. Explanations for the calculated barriers based on structural data are offered.

Keywords: Olefin dimerization; Olefin insertion; Homogeneous catalysis; Density functional theory; Computational chemistry

1. Introduction

The nickel(II)-catalyzed 1-butene dimerization is an important type of reaction for industrial purposes. Several processes of relevance have been developed over the years. In the Shell higher olefins process developed by Keim and co-workers [1–4], α -olefins are produced using a self-activated P,O-catalyst. In the Dimersol-X process developed by Chauvin [5, 6], a propene/1-butene mixture is dimerized using AlEtCl₂ to activate the nickel(II)-phosphine catalyst. Finally, the heterogeneous Octol process [7, 8] employs a NiO over Al₂O₃/SiO₂ catalyst system for the 1-butene dimerization. The resulting C₈-dimer products of this

*Corresponding author. Email: wolfgang.hieringer@fau.de

Dedicated to Rudi van Eldik on the occasion of his 70th birthday.

reaction are n-octane, 3-methyl-heptane, and 3,4-dimethylhexane. The C₈-products are used for C₉-plasticizer production. Hence, a low degree of branching of the C₈-mixture is desired [8, 9]. Besides, the highly successful phosphine catalysts, which are used in the Dimersol process, classical spectator ligands like the N-heterocyclic carbene or the O,O-chelating hexafluoroacetylacetonate (hfacac) [9] system are among the most successful systems for the nickel-catalyzed 1-butene dimerization. Moreover, since 1990 imidazolium-based ionic liquids (i.e. [BMIM]⁺[AlCl₄][−]) are successfully used as alternative solvents for the nickel-catalyzed olefin dimerization [10]. The possible benefit of such solvents in homogeneous catalysis has been demonstrated in several processes before, such as increased catalytic activities or simplified catalyst recycling [9, 10].

The commonly accepted nickel(II)-hydride mechanism [11, 12] is shown in figure 1. The reaction consists of the following elemental steps: (i) olefin insertion (hydrometalation) into a Ni–H bond (**1** → **2**), (ii) 1-butene coordination (**2** → **3**), (iii) olefin insertion into the Ni–C_{butyl} σ-bond (**3** → **4**), (iv) 1-butene coordination (**4** → **5**), and (v) chain termination via a two-step β-hydride transfer (**5** → **6** → **7**), which has been found to be favored over a β-hydride elimination in previous theoretical studies [12–14]. The 1-butene insertion step (**3** → **4**) was established as the step [12] with the highest barrier and can thus be considered as the crucial step of the catalytic cycle.

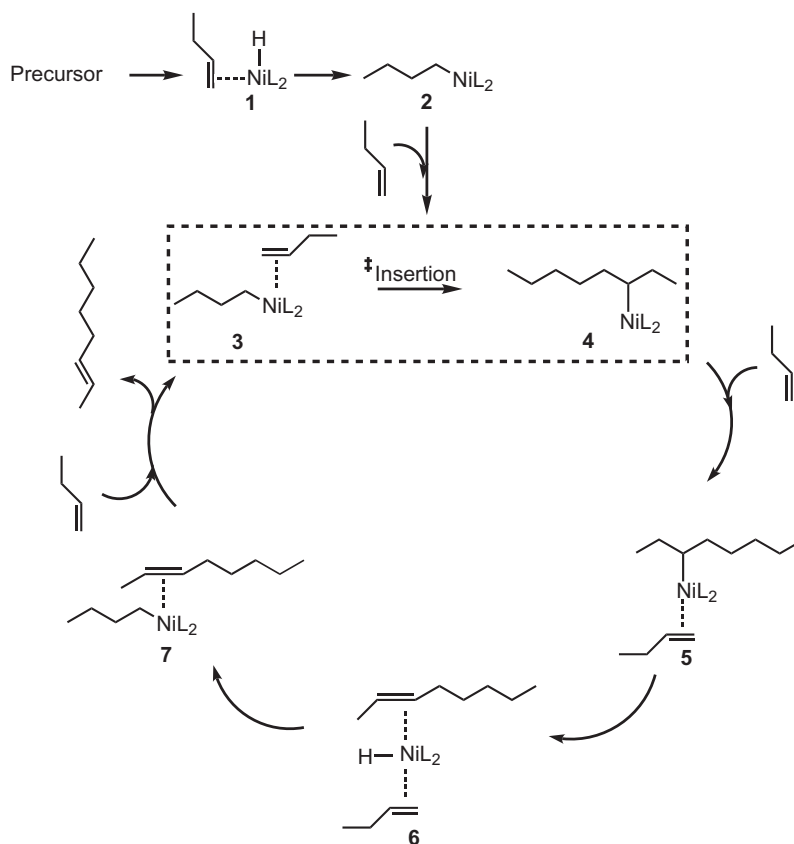


Figure 1. Considered catalytic cycle for the nickel(II)-catalyzed 1-butene dimerization [11].

In this study, we focus on the insertion step ($3 \rightarrow 4$) of a nickel(II) phosphine catalyst in the presence of a $[\text{BMIM}]^+[\text{AlCl}_4]^-$ ionic liquid environment. We discuss the possibility of anion (i.e. AlCl_4^-) coordination to the nickel center of the catalyst in competition to triphenylphosphine (PPh_3) coordination. Subsequently, we explore the effect of the coordination sphere at the Ni center on the activation barriers for butene insertion. This will shed light on the possible nature of the active species of the Ni catalyst in ionic liquid solution.

2. Computational details

Density functional theory [15] calculations were carried out using the program package Turbomole [16, 17]. In general, unless stated otherwise, the gradient-corrected exchange-correlation functional due to Becke [18] and Perdew [19] (denoted BP) was used throughout in combination with the polarized triple zeta split-valence basis set def2-TZVP [20] and the associated auxiliary basis set for the *resolution of the identity* technique [21]. Full-geometry optimizations and transition state searches without symmetry or other constraints have been performed at this level (BP/TZVP//BP/TZVP). Vibrational frequency calculations have been performed to verify the nature of the stationary points at this level. All reaction and activation energies generally correspond to electronic energy differences unless stated otherwise; zero-point vibrational energy corrected values as well as free energy differences can be found in the Supplemental data file. In certain cases as specified below, the conductor-like screening model (COSMO) [22] has been used in order to approximately simulate the ionic liquid environment. A dielectric constant of $\epsilon = 12$, which has been found characteristic for imidazolium-based ionic liquids [23], has been used in these calculations.

For the calculation of activation barriers, additional levels of theory have been applied to verify the results. Corresponding data are given in the Supplemental data. To test the influence of van der Waals dispersion on the barriers, reactants and transitions states have been re-optimized with the third-generation dispersion correction due to Grimme [24] (D3, overall notation BP-D3/TZVP//BP-D3/TZVP). The dispersion effects substantially changed some of the barriers (by up to roughly 5 kcal mol^{-1}), but the relative ordering of activation barriers for the different catalyst species remained roughly the same (see the Supplemental data for details). To test the influence of possible solvent effects, additional single-point calculations of the BP-optimized geometries have been performed with the COSMO model (BP(COSMO)/TZVP//BP/TZVP level). It turned out, however, that the COSMO effect was small, with changes in activation energy usually below 1 kcal mol^{-1} compared to the gas-phase calculations. Corresponding data are given in the Supplemental data. In addition, the barrier heights have also been recalculated with the B3LYP functional [25] using the BP-optimized geometries (B3LYP/TZVP//BP/TZVP). As shown in the Supplemental data, these calculations yielded similar barriers as with the BP functional within approximately 1 kcal mol^{-1} , in agreement with previous observations [12] on similar systems. Hence, all activation barriers and geometry data quoted here correspond to the BP/TZVP level, while the results of the other levels of theory can be found in the Supplemental data file.

For the ligand-exchange equilibria (see figures 2 and 3), solvent effects are expected to be of major importance due to the involvement of ionic species. Therefore, in this case, all geometries have been optimized including COSMO, i.e. all energies given in this context correspond to the BP(COSMO)/TZVP//BP(COSMO)/TZVP level. For comparison, also here the results have additionally been verified with single-point B3LYP(COSMO) calculations

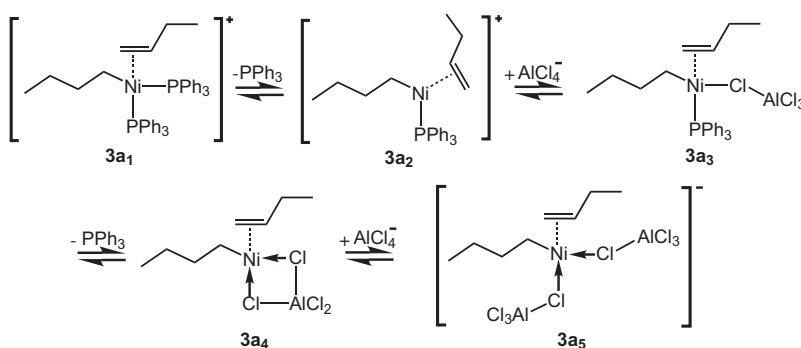


Figure 2. Considered catalyst compositions for insertion reactant **3a** in the presence of triphenyl phosphine and $[\text{AlCl}_4]^-$ ligands.

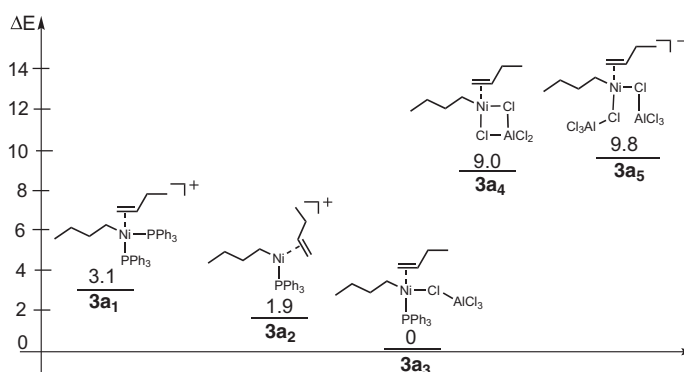


Figure 3. Relative energies of catalyst compositions **3a** in kcal mol^{-1} , BP(COSMO)/TZVP level; (R, R' = butene, butyl).

using the BP(COSMO) geometries, see the Supplemental data (figure S1 and table S6 [see online supplemental material at <http://dx.doi.org/10.1080/00958972.2015.1075015>]) for details. It turned out that the same low-energy species were predicted with this functional, although the calculated energy levels differ significantly from those predicted at the BP level.

All complexes were treated as closed-shell (spin-singlets); test calculations on selected species indicate that the corresponding triplet states are higher in energy by at least 20 kcal mol^{-1} . This is in agreement with previous observations [12].

3. Results and discussion

3.1. Relative energies of catalyst species

As a first step, the thermodynamic accessibility of the different catalyst compositions was estimated based on the relative energies of the considered species, see figure 2. The catalyst species can be coordinated either by the triphenylphosphine ligands (species **3a1** and **3a2** in

figure 2) and/or by the anion of the ionic liquid solvent. In this study, we consider AlCl_4^- as the anion of the ionic liquid, which is part of the common $[\text{BMIM}]^+[\text{AlCl}_4]^-$ ionic liquid. If anion coordination is considered, three more catalyst complexes can be considered, featuring one ($\mathbf{3a}_3$, $\mathbf{3a}_4$) or even two anions ($\mathbf{3a}_5$) in the coordination sphere (figure 2).

In the case of $\mathbf{3a}_1$ and $\mathbf{3a}_3$ – $\mathbf{3a}_5$, the nickel(II) center possesses a 16 valence-electron configuration. On the other hand, complex $\mathbf{3a}_2$ possesses a 14 VE configuration due to the lack of an additional ligand. To our knowledge, such an unsaturated nickel(II) complex has never been considered before for the olefin insertion step. There are several theoretical studies of nickel(II)-catalyzed olefin dimerization considering bidentate ligand systems. In these studies, the calculated chelating ligands were either symmetrical ($\text{O}^{\wedge}\text{O}$, $\text{N}^{\wedge}\text{N}$) [13, 14, 26, 27] or asymmetrical ($\text{P}^{\wedge}\text{N}$, $\text{P}^{\wedge}\text{O}$, $\text{N}^{\wedge}\text{O}$) [28–30].

Figure 3 shows the calculated relative energies of all the species shown according to the equilibria in figure 2. At the present computational level, nickel complexes including at least one phosphine ligand ($\mathbf{3a}_1$, $\mathbf{3a}_2$, $\mathbf{3a}_3$) are energetically favored by more than 5 kcal mol⁻¹ over the phosphine-free complexes ($\mathbf{3a}_4$, $\mathbf{3a}_5$) which only bear one or two AlCl_4^- ligands. In particular, the calculations suggest that species $\mathbf{3a}_3$ which has one phosphine ligand and one AlCl_4^- ligand in its coordination sphere is lowest in energy and thus should be the dominant species in the system. Please note, however, that the present calculations should only be considered indicative since the details of the solvation of the complexes in the ionic liquid cannot be fully captured using the COSMO approach, and entropy effects have been neglected (additional data from the B3LYP functional as well as gas-phase zero-point vibrational energy and entropy corrections can be found in the Supplemental data). Nevertheless, the present data indicate that anion coordination should be taken into consideration in $[\text{BMIM}]^+[\text{AlCl}_4]^-$ solution.

3.2. Activation energies for butene insertion

We now address the activation barriers for butene insertion for the five different catalyst species discussed in the previous section, cf figure 2. For each of these species, the four insertion pathways [12] shown in figure 4 have been considered. The calculated barriers are summarized in table 1 (see the Supplemental data for additional data from other levels of theory).

Upon insertion, a C–C single bond and a β -agostic Ni–H interaction are formed at the expense of a C–C double bond and a nickel-butene π -bond. The coordinated butene ligand can insert into a primary or a secondary Ni–C bond ($\mathbf{3a}$, $\mathbf{3b}$) in two different orientations each, resulting in a total of four different insertion products ($\mathbf{4a}$ – $\mathbf{4d}$) as shown in figure 4. In each case, the reaction passes through a four-centered transition state. The four pathways are labeled **a**–**d** in this work, cf figure 4. Steps **a** and **b** represent a 1-butene insertion into a primary butyl group, whereas pathways **c** and **d** represent an insertion into a secondary butyl group.

Table 1 shows that, of all the systems considered, species $\mathbf{3a}_2$ (cf figure 2) which bears a single phosphine ligand has the lowest activation barriers for butene insertion between 8.5 and 11.5 kcal mol⁻¹ for all pathways (**a**–**d**). This species can thus be considered as the catalytically most active. The calculated barriers are slightly lower for paths **a** and **b**, i.e. for insertion into a primary butyl–Ni bond compared to insertion into a secondary butyl–Ni bond.

Somewhat higher activation barriers are calculated for the homoleptic bis-phosphine catalyst $\mathbf{3a}_1$ and the mixed-ligand species $\mathbf{3a}_3$. The barriers for the phosphine-free species $\mathbf{3a}_4$ and $\mathbf{3a}_5$, on the other hand, are calculated to be higher by about 10 kcal mol⁻¹ compared to

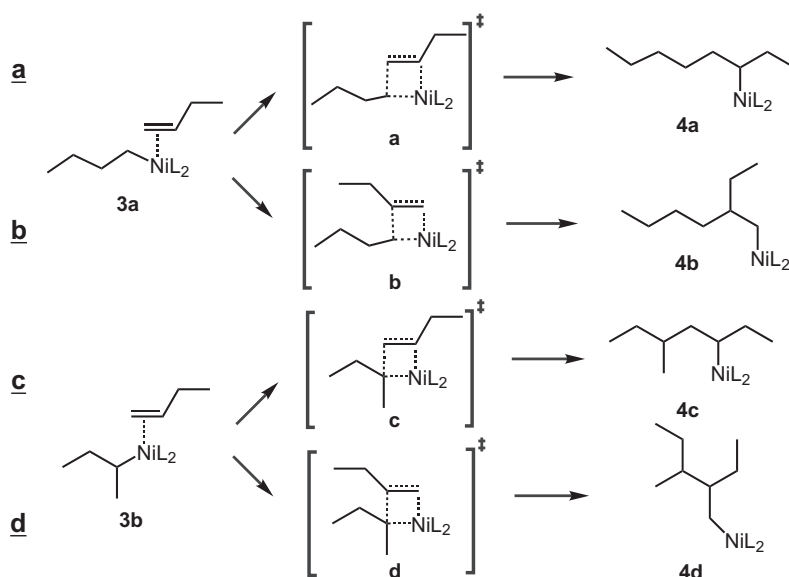


Figure 4. Regioselectivity of the insertion step (cf Ref. [12]) of the nickel-catalyzed 1-butene dimerization, starting from a primary butyl complex **3a** or a secondary butyl complex **3b**, respectively; the butene ligand can insert into the Ni–C bond via a four-centered transition state in two different orientations for each **3a** and **3b**, resulting in a total of four possible insertion pathways, each of which yielding a different insertion product **4a–4d**; L = (PPh₃, [AlCl₄][−]).

Table 1. Calculated activation energies for the butene insertion pathways (a–d) shown in figure 4 and for different ligand spheres (1–5), cf figure 2, in kcal mol^{−1}; BP/TZVP level.

Insertion path	1 (L = 2x PPh ₃)	2 (L = PPh ₃)	3 (L, L' = PPh ₃ , AlCl ₄ [−])	4 (L = AlCl ₄ [−])	5 (L = 2x AlCl ₄ [−])
a	13.2	8.5	12.9	18.8	19.2
b	10.5	8.9	11.5	20.4	20.8
c	13.4	10.6	13.1	20.3	19.7
d	14.3	11.5	11.9	22.1	23.2

the phosphine-coordinated species **3a**₂, and also significantly higher than **3a**₁ and **3a**₃. Remember that these species were also calculated to be thermodynamically disfavored, cf Section 3.1.

Our present data thus suggest that a “ligandless” catalyst system (i.e. without classical ligands such as phosphine) in which only the AlCl₄[−] anions of the ionic liquid solvent can act as ligands to the nickel catalyst should be less active than a phosphine-containing system. In other words, the presence of classical ligand (triphenylphosphine in the present case) seems to be beneficial for the activity of the catalyst.

3.3. Optimized geometries of intermediates and transition states

To gain a better understanding of the calculated barriers, we now analyze the calculated geometries of the insertion educts **3a** and the corresponding transition states (figure 4). The

questions which we will address are the following. (i) What distinguishes the most active mono-phosphine complex **3a₂** from its competitors? (ii) Why is olefin insertion kinetically favored for the phosphine-bearing complexes **3a₁**–**3a₃** compared to the phosphine-free systems **3a₄**, **3a₅**?

Only pathway **b** (cf figure 4) will be discussed in detail, which was selected for the discussion because it shows the lowest insertion barrier for L, L' = PPh₃ (Comparable results are obtained for pathway **a**, see tables 2 and 3. Structural data on the other pathways can be found in the Supplemental data). Furthermore, it suffices to restrict our discussion to the diphosphine complex **3a₁**, the mono-phosphine complex **3a₂**, and the η^2 -AlCl₄ complex **3a₄**. The structural characteristics of the mixed-ligand complex **3a₃** resemble those of **3a₁**, while the essential characteristics of **3a₅** resemble those of **3a₄** (again, see the Supplemental data for structural data).

The diphosphine reactant complex **3a₁** (figure 5, left) shows a roughly tetrahedral coordination geometry at the Ni center (i.e. when counting the η^2 bound olefin and the butyl as one ligand each). The Ni–butyl σ -bond is enhanced via a β -agostic interaction. Importantly, the π -bond of the butene ligand (C₁–C₂, see figure 5) is oriented *perpendicular* to the Ni–C₃ bond into which it will be inserted in the course of the reaction (cf figure 5).

In the transition state **TS-b₁** (figure 5 right), on the other hand, the butene π -bond is reoriented such that it is now almost *parallel* to the Ni–C₃ bond. The coordination geometry at the Ni center can be described as in between tetrahedral and square planar. Most notably, the β -agostic bond of the reactant complex has been replaced by an α -agostic interaction in the transition state. Such α -agostic interactions are usually less favorable due to more unfavorable bond angles which are required by the resulting three-ring structure. In the transition state, a β -agostic interaction appears to be unfavorable due to the almost planar arrangement of the three C atoms and the Ni atom in the four-centered transition state. Hence, the β -agostic interaction of the reactant complex apparently cannot be preserved in the transition state for geometric reasons (similar observations are made for the heteroleptic complex **3a₃**; see the Supplemental data for details).

The situation for the mono-phosphine complex **3a₂** is qualitatively different from that of the diphosphine complex, see figure 6. In the reactant, the butene π -bond (C₁–C₂) is already in an almost parallel orientation relative to the Ni–C₃ bond where it will be inserted. The overall coordination geometry is essentially planar already in the reactant complex. Consequently, when going from **3a₂** to the transition state **TS-b₂**, only minor structural reorganizations are necessary. As before, in the transition state, the coordination geometry remains almost planar at the Ni center. However, the β -agostic interaction of the reactant is *preserved* in the transition state **TS-b₂**.

Table 2. Salient bond lengths for the reactant complexes **3a₁** (L, L' = PPh₃) and **3a₄** (L = [AlCl₄][−]) as well as for the corresponding transition states **TS-a₁**, **TS-b₁**, **TS-a₄**, and **TS-b₄** in Å; cf figures 5, 7, and the Supplemental data.

Pathway	$r(\text{C}_1\text{--Ni})$	$r(\text{C}_3\text{--Ni})$	$r(\text{C}_1\text{--C}_2)$	$r(\text{Ni--H}_1)$	$r(\text{Ni--H}_2)$	$r(\text{C}_2\text{--C}_3)$
3a₁	2.09	1.97	1.39	1.87	—	—
3a₄	1.99	1.91	1.41	2.01	—	—
TS-a₁	1.99	2.15	1.44	—	2.10	2.12
TS-b₁	1.98	2.12	1.44	—	2.01	2.12
TS-a₄	1.94	2.05	1.46	—	1.94	1.95
TS-b₄	1.90	2.07	1.46	—	1.92	1.95

Table 3. Changes of selected bond lengths from the reactant to the transition state for the bisphosphine (**3a₁**) and the AlCl₄ catalyst (**3a₄**), in Å; cf table 2 for absolute distances.

Pathway	$\Delta r(\text{C}_1\text{--Ni})$	$\Delta r(\text{C}_3\text{--Ni})$	$\Delta r(\text{C}_1\text{--C}_2)$
3a₁ → TS-a₁	−0.10	+0.18	+0.05
3a₁ → TS-b₁	−0.11	+0.15	+0.05
3a₄ → TS-a₄	−0.05	+0.14	+0.05
3a₄ → TS-b₄	−0.09	+0.16	+0.05

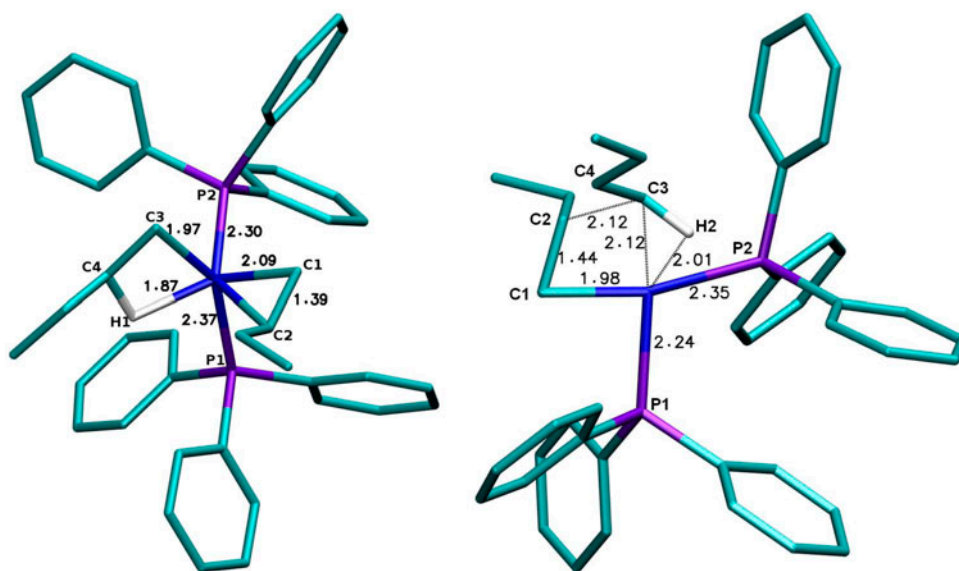


Figure 5. Optimized geometries for insertion pathway **b** and L, L' = PPh₃; reactant **3a₁** (left), transition state **TS-b₁** (right). Color code: Ni = dark blue, P = violet, C = light blue, and H = white; numbers represent bond distances (in Å) of ligator atoms (H, C, P) to Ni; all but the agostic hydrogen atoms are omitted (see <http://dx.doi.org/10.1080/00958972.2015.1075015> for color version).

Hence, from a comparison of the geometries of the diphosphine with the mono-phosphine catalyst complex, the following can be concluded. In the mono-phosphine system, the reactant complex structurally already resembles the transition state for butene insertion, and only minor structural adjustments are necessary to reach the transition state. In the diphosphine complex, larger structural rearrangements are necessary. These stereoelectronic effects thus qualitatively explain the lower barrier computed for butene insertion for **3a₂** compared to **3a₁**.

The remaining question is as to why the barrier for the phosphine-free catalyst complexes **3a₄** and **3a₅**, which are only coordinated by one or two AlCl₄[−] ligands rather than phosphine, is substantially higher than for the complexes bearing at least one phosphine ligand. The optimized geometries of **3a₄** and **TS-b₄** are shown in figure 7 (corresponding data on **3a₅** and **TS-b₅** can be found in the Supplemental data).

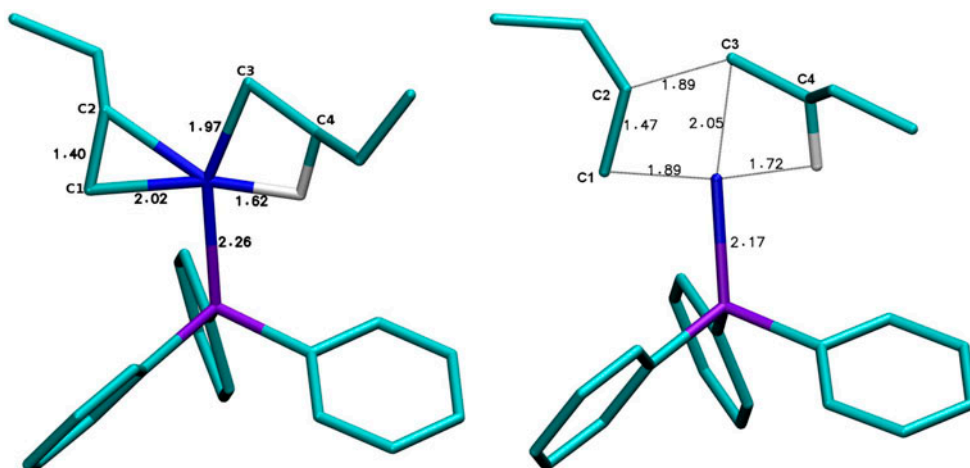


Figure 6. Optimized geometries for insertion pathway **b** for the mono-phosphine complex; reactant **3a₂** (left), transition state **TS-b₂** (right). Color code: Ni = dark blue, P = violet, C = light blue, and H = white; numbers represent bond distances (in Å) of ligator atoms (H, C, P) to Ni; all but the agostic hydrogen atoms are omitted (see <http://dx.doi.org/10.1080/00958972.2015.1075015> for color version).

We note that the reactants and transition states overall show largely similar features for both ligand spheres in **3a₁** and **3a₄** (or **3a₅**, cf figures 5 and 7). Both reactant complexes show a roughly tetrahedral geometry at the Ni center. Again, the butyl–Ni σ -bond is supplemented by a β -agostic interaction, and the π -bond of the butene ligand is perpendicularly oriented with respect to the Ni–butyl bond. As before, the transition states of both ligand spheres show α -agostic interactions rather than β -agostic bonds, and the (former) π -bond readies itself for insertion by orienting parallel to the Ni–butyl σ -bond which is about to be

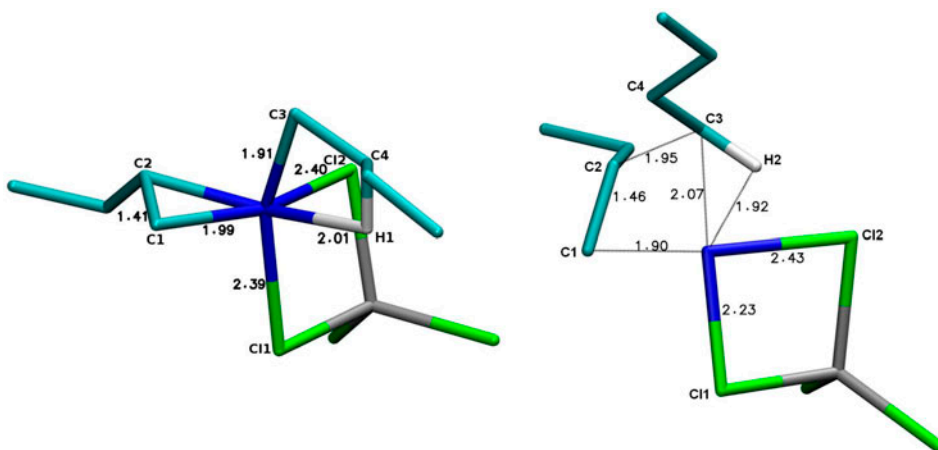


Figure 7. Optimized geometries for insertion pathway **b** and $L = \text{AlCl}_4^-$; reactant **3a₄** (left), transition state **TS-b₄** (right). Color code: Ni = dark blue, Cl = green, C = light blue, and H = white; numbers represent bond distances (in Å) of ligator atoms (H, C, Cl) to Ni; all but the agostic hydrogen atoms are omitted (see <http://dx.doi.org/10.1080/00958972.2015.1075015> for color version).

broken in **TS-b₄**. Hence, similar stereoelectronic arguments as in the diphosphine complex can be used for **3a₄** as well.

The key to understand the higher activation energy of the phosphine-free complex **3a₄** compared to **3a₁** lies in the two Ni–C bond lengths and, in particular, in their changes in the course of the reaction. Table 2 shows some of the critical bond lengths for both complexes. The Ni–C distances are *shorter* in **3a₄** than in the phosphine complex **3a₁** by 0.06 and 0.1 Å. We tentatively attribute this to the different charges of the complexes (cationic vs. neutral), to steric effects, as well as to the presumably weaker coordination of the chlorine atoms in AlCl_4^- to the Ni center compared to the phosphines. The latter also may be viewed as a manifestation of a *trans* influence, where phosphines typically exert a stronger *trans*-labilizing effect than halides. The same trend in bond lengths also holds for the transition states: **TS-b₄** exhibits shorter Ni–C distances than **TS-b₁**. Overall, the shorter distances indicate stronger Ni–C bonds in **3a₄** compared to **3a₁**.

The key observation now lies in the *changes* of the Ni–C distances from the reactants to the corresponding transition states, see table 3. On the way to the transition state, the Ni–C₁ distance, which corresponds to the newly formed Ni–C bond, contracts by roughly 0.1 Å (**3a** → **TS-b**) for *both* ligand spheres, while the Ni–C₃ distance of the Ni–butyl bond that is being broken increases by about 0.15 Å for both ligand spheres. In other words, the structural changes on the way from the reactants to the transition states are essentially the same for both **3a₁** and **3a₄** (as long as only the Ni–C distances are considered).

We now conjecture that it will be energetically more “expensive” to increase the lengths of the stronger Ni–C₃ bonds found in **3a₄** compared to those in **3a₁** by (roughly) the same amount (table 3). In simpler words, this means that the Ni–C bonds to be broken are somewhat “looser” in the diphosphine complex **3a₁** than in **3a₄**, and hence the transition state is more easily formed in **3a₁** than in **3a₄**, thus facilitating the reaction of **3a₁** (in essence, this alludes to the parallelity of bond distances and vibrational frequencies that is commonly observed in transition metal complexes). In summary, these structural changes offer a possible explanation of the higher activation barriers for butene insertion found for the phosphine-free complexes **3a₄** (and **3a₅**) as compared to phosphine complexes such as **3a₁**.

Another notable geometrical point concerns the newly forming C–C bonds in the transition states **TS-b₁** and **TS-b₄**. The C₂–C₃ distance of **TS-b₁** is 2.12 Å, whereas that of **TS-b₄** amounts to $r(\text{C}_2\text{--C}_3) = 1.95$ Å (table 2, last column). This means that **TS-b₄** is “later” on the insertion path, i.e. the formation of the new C–C bond is more advanced along the phosphine-free path (**TS-b₄**) than along the insertion path of the bisphosphine complex (**TS-b₁**). This is consistent with the calculated reaction energies: $\Delta E_{3a_1 \rightarrow 4b_1} = -24.5$ kcal mol^{−1}, $\Delta E_{3a_4 \rightarrow 4b_4} = -2.5$ kcal mol^{−1}. The insertion reaction via the bisphosphine complex **3a₁** is significantly more exothermic than that via the phosphine-free complex **3a₄**, which is, as expected, also reflected in the transition structures.

4. Conclusion

In this study, the butene insertion step of the nickel-catalyzed butene dimerization in $[\text{BMIM}]^+[\text{AlCl}_4]^-$ ionic liquid solution and in the presence of triphenyl phosphine ligands has been considered. Special attention was given to the possibility of anion coordination to the nickel phosphine catalyst. Using density functional theory, the relative energies of various hypothetical active catalyst species and associated activation barriers for butene

insertion have been calculated. The results show that the energetically most favorable species is a heteroleptic complex with a phosphine and an AlCl_4^- ligand coordinated to the nickel center. Other phosphine-bearing complexes are predicted to have slightly higher energies. However, the lowest activation barrier for butene insertion is not found for this mixed-ligand species, but for a mono-phosphine complex without anion coordination. This complex is only slightly higher in energy than the mixed-ligand species. The calculations furthermore show that phosphine-free catalyst complexes, which are exclusively coordinated by one or two AlCl_4^- anions, both are high in energy and also show higher activation barriers for butene insertion, compared to complexes with at least one coordinated phosphine ligand. Differences in the calculated activation barriers can be rationalized by considering stereoelectronic effects such as the necessity to reorient the olefin with respect to the Ni–C bond to reach the transition state for olefin insertion. The present calculations thus suggest that anion coordination to the nickel catalyst should be taken into account in the presence of the $[\text{BMIM}]^+[\text{AlCl}_4]^-$ ionic liquid. They also suggest, however, that phosphine ligands are both needed to stabilize the active species thermodynamically and to ensure a low activation barrier for butene dimerization.

To further corroborate these initial results, the study should be extended to other ligand/ionic liquid combinations. The present study has focused on the classical triphenyl phosphine ligands and a common ionic liquid, $[\text{BMIM}]^+[\text{AlCl}_4]^-$, only. Furthermore, it would be desirable to take the dynamic properties of the ionic liquid solvent into account explicitly because this will give access to meaningful and presumably important entropic contributions. The results of the present and follow-up studies may thus eventually aid in the development of efficient catalyst systems for butene dimerization with optimal ligand/ionic liquid combinations.

Acknowledgements

We thank the Deutsche Forschungsgemeinschaft (DFG) for funding through the Cluster of Excellence “Engineering of Advanced Materials” located at the University of Erlangen (www.eam.uni-erlangen.de). We also thank Marco Haumann for helpful comments on the manuscript.

Disclosure statement

No potential conflict of interest was reported by the authors.

References

- [1] M. Peuckert, W. Keim. *Organometallics*, **2**, 594 (1983).
- [2] W. Keim, *Chem. Ing. Tech.*, **56**, 850 (1984).
- [3] B. Cornils, W.A. Herrmann. *Applied Homogeneous Catalysis with Organometallic Compounds*, Wiley-VCH, Weinheim (2000).
- [4] W. Keim. *Ed. Angew. Chem. Int.*, **29**, 235 (1990).
- [5] Y. Chauvin, J. Gaillard, D. Quang, J. Andrews. *Chem. Ind. (London)*, **1**, 375 (1974).
- [6] B. Bogdanović, B. Henc, H.-G. Karmann, H.-G. Nüssel, D. Walter, G. Wilke. *Ind. Eng. Chem.*, **62**, 34 (1970).
- [7] S. Albrecht, D. Kiessling, D. Maschmayer, F. Nierlich, G. Wendt. *Chem. Ing. Tech.*, **77**, 695 (2005).

- [8] A. Brückner, U. Bentrup, H. Zanthoff, D. Maschmeyer. *J. Catal.*, **266**, 120 (2009).
- [9] B. Ellis, W. Keim, P. Wasserscheid. *Chem. Commun.*, 337 (1999).
- [10] (a) Y. Chauvin, B. Gilbert, I. Guibard. *J. Chem. Soc. Chem. Commun.*, 1715 (1990); (b) Y. Chauvin, S. Einloft, H. Olivier-Bourbigou. *Ind. Eng. Chem. Res.*, **34**, 1149 (1995); (c) P. Wasserscheid, W. Keim. *Angew. Chem.*, **112**, 3926 (2000); (d) P. Wasserscheid, M. Eichmann. *Cat. Today*, **66**, 309 (2001); (e) H. Olivier-Bourbigou, L. Magna. *J. Mol. Catal.*, **182–183**, 419 (2002); (f) M. Eichmann, W. Keim, M. Haumann, B.U. Melcher, P. Wasserscheid. *J. Mol. Catal.*, **314**, 42 (2009).
- [11] W. Keim. *New J. Chem.*, **11**, 531 (1987).
- [12] I. Nikiforidis, A. Görling, W. Hieringer. *J. Mol. Catal. A.*, **341**, 63 (2011).
- [13] L. Fan, A. Krzywicki, A. Somogyvari, T. Ziegler. *Inorg. Chem.*, **33**, 5287 (1994).
- [14] L. Fan, A. Krzywicki, A. Somogyvari, T. Ziegler. *Inorg. Chem.*, **35**, 4003 (1996).
- [15] W. Koch, M. Holthausen. *A Chemist's Guide to Density Functional Theory*, 2nd Edn, Wiley-VCH, Weinheim (2000).
- [16] R. Ahlrichs, M. Bär, M. Häser, H. Horn, C. Kölmel. *Chem. Phys. Lett.*, **162**, 165 (1989).
- [17] *TURBOMOLE 6.3*, University of Karlsruhe, Germany (1988). Available online at: www.turbomole.com.
- [18] A. Becke. *Phys. Rev. A*, **38**, 3098 (1988).
- [19] J. Perdew. *Phys. Rev. B*, **33**, 8822 (1986).
- [20] F. Weigend, R. Ahlrichs. *Phys. Chem. Chem. Phys.*, **7**, 3297 (2005).
- [21] K. Eichkorn, O. Treutler, H. Öhm, M. Häser, R. Ahlrichs. *J. Chem. Phys.*, **240**, 283 (1995).
- [22] A. Klamt, G. Schnnrmann. *J. Chem. Soc. Perkin Trans. 2*, **5**, 799 (1993).
- [23] C. Daguenet, P.J. Dyson, I. Krossing, A. Oleinikova, J. Slattery, C. Wakai, H. Weingärtner. *J. Phys. Chem.*, **110**, 12682 (2006).
- [24] S. Grimme, J. Antony, S. Ehrlich, H. Krieg. *J. Chem. Phys.*, **132**, 151104 (2010).
- [25] A. Becke. *J. Chem. Phys.*, **98**, 5648 (1993).
- [26] S. Strömberg, K. Zetterberg, P. Siegbahn. *Dalton Trans.*, 4147 (1997).
- [27] D. Musaev, M. Svensson, K. Morokuma. *Organometallics*, **16**, 1933 (1997).
- [28] V. Tognetti, P. Floch, C. Adamo. *J. Comput. Chem.*, **31**, 1053 (2009).
- [29] F. Hasanayn, P. Achord, P. Braunstein, H. Magnier, K. Krogh-Jespersen, A. Goldman. *Organometallics*, **31**, 4680 (2012).
- [30] M. Chan, L. Deng, T. Ziegler. *Organometallics*, **19**, 2741 (2000).